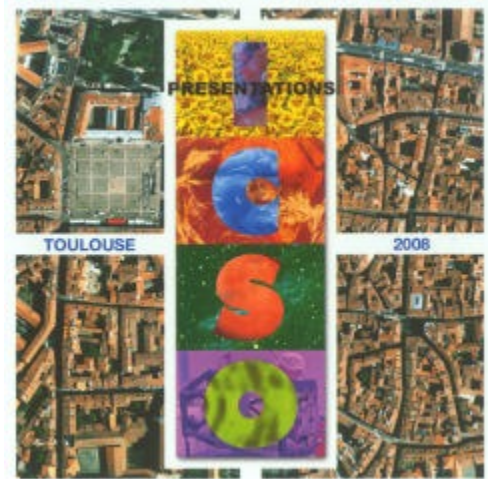


International Conference on Space Optics—ICSO 2008

Toulouse, France

14–17 October 2008

Edited by Josiane Costeraste, Errico Armandillo, and Nikos Karafolas



ALISEO on MIOsSat: an imaging interferometer for earth observation

A. Barducci

F. Castagnoli

G. Castellini

D. Guzzi

et al.



ALISEO ON MIOSAT: AN IMAGING INTERFEROMETER FOR EARTH OBSERVATION

A. Barducci, F. Castagnoli, G. Castellini, D. Guzzi, P. Marcoionni, *I. Pippi

CNR – IFAC, Via Madonna del Piano 10, 50019 Sesto Fiorentino, ITALY
Tel.: +39 0555226301, Fax: +39 0555226348, *E-mail: L.Pippi@ifac.cnr.it

ABSTRACT

The Italian Space Agency (ASI) decided to perform a low cost Earth observation mission based on a new mini satellite named MIOsat which will carry various technological payloads. Among them an imaging interferometer designed and now ready to be assembled and tested by our Institute.

The instrument, named ALISEO (Aerospace Leap-frog Imaging Stationary interferometer for Earth Observation), operates in the common-path Sagnac configuration, and it does not utilize any moving part to scan the phase delays between the two interfering beams. The sensor acquires target images modulated by a pattern of autocorrelation functions of the energy coming from each scene pixel, and the resulting fringe pattern remains spatially fixed with respect to the instrument's field-of-view. The complete interferogram of each target location is retrieved by introducing a relative source-observer motion, which allows any image pixels to be observed under different viewing-angles and experience discrete path differences.

The paper describes the main characteristics of the imaging interferometer as well as the overall optical configuration and the electronics layout. Moreover some theoretical issues concerning sampling theory in "common path" imaging interferometry are investigated. The experimental activity performed in laboratory is presented and its outcomes are analysed. Particularly, a set of measurements has been carried out using both standard (certificate) reflectance tiles and natural samples of different volcanic rocks. An algorithm for raw data pre-processing aimed at retrieving the at-sensor radiance spectrum is introduced and its performance is addressed by taking into account various issues such as dark signal subtraction, spectral instrument response compensation, effects of vignetting, and Fourier back-transform. Finally, examples of retrieved absolute reflectance of several samples are sketched at different wavelengths.

1. INTRODUCTION

A low cost technological mission for Earth observation, based on the new mini-satellite MIOsat, was decided by the Italian Space Agency. Among

different payloads, an imaging interferometer was selected as an innovative optical instrument for remote sensing applications.

The mission and payload requirements are listed in the tables 1 and 2.

MIOsat operational characteristics	
Orbit	polar, sun-synchronous
Descending node	9:30 - 10:30 a.m. local time
Altitude	500 Km
Expected life-time	2-3 years
Size	1m x 1m x 1m
Mass	Less than 130 Kg
Power	Less than 150 W

Table 1. MIOsat mission characteristics

ALISEO main characteristics	
Detector	Silicon CCD 2D-array (1024 x 1024 elements)
Spectral range	400 - 1000 nm
Spectral resolution	Better than 5 nm @ 650 nm
Swath	10 Km
FOV	1.15°
Spatial resolution	10 m
Digitalization	12 bit
Expected SNR	200 @ 650 nm
Size	60 cm (along flight direction) x 30 cm (along nadir axis) x 30 cm
Weight	Less than 20 Kg
Power	Less than 25 W

Table 2. ALISEO main characteristics

A preliminary study on the imaging interferometry for remote sensing applications, assessed by ASI to our Institute, demonstrated the feasibility of such instrumentation for Earth observation from space. Advantages and disadvantages with respect to imaging spectrometers using dispersive components were also investigated.

Among them, a valuable advantage of imaging interferometers is their ability to change the sampled spectral range and their resolving power by simply adjusting the sensor sampling step and the instrument Field-Of-View (FOV) [1], [2], [3]. An additional advantage is connected with the possible exclusion of the input slit, which strongly reduces the power

admitted in dispersive spectrometers. Critical points are associated with the heavy data pre-processing necessary for compensating the instrument response and possible acquisition artefacts [4]. Moreover, due to the nature of the interferograms, it is crucial acquire the data at the highest accuracy [5].

On the basis of that preliminary study our Institute performed the Phase A and B of the ALISEO payload which will be integrated on MIOsat.

2. ALISEO INSTRUMENT CONCEPT

ALISEO acquires the image as modulated by a pattern of autocorrelation functions of the energy coming from the observed scene. The complete interferogram of any target locations is observed introducing relative source-observer motion, which allows each pixel to be observed while going across the entire pattern of ElectroMagnetic (EM) autocorrelation function.

ALISEO consists of the following devices: fore-optics, Sagnac interferometer, imaging optics, detector and electronics.

The optical layout of the Sagnac interferometer is shown in the Fig. 1.

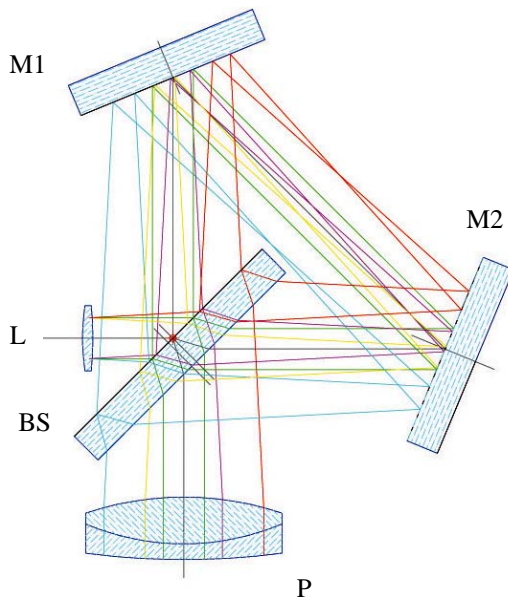


Fig. 1 Interferometer optical layout

Light is collected from the objective L, then the two interfering rays are generated by the beam-splitter

BS and travel the triangular ray path in opposite directions by means of two folding mirrors M1 and M2. The two rays are then focused onto the CCD by the camera lens P.

It is easy to demonstrate that the BS is the fundamental component, which provides the basic phase-delay between the two coherent rays. Nonetheless, it can be shown that phase-delay is heavily affected by the overall instrument geometry: the BS to M1 and M2 distances and the orientation of the two folding mirrors.

A critical problem in the above configuration is the wide dimensions required for the beam-splitter and the two folding mirrors M1 and M2. In order to reduce their dimensions an afocal telescope was considered as input element. The primary input telescope is made up of two off-axis con-focal parabolic mirrors that reduce of a factor 3.7 the diameter of the input beam.

The layout of the optical system which includes fore-optics, Sagnac interferometer and imaging optics is shown in Fig.2.

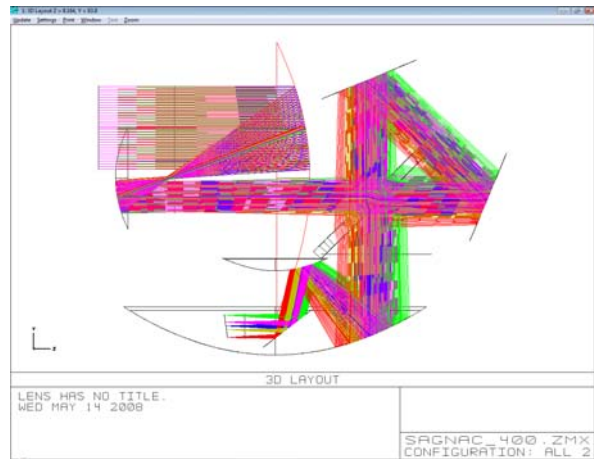


Fig. 2: Optical system layout

Fig. 3 shows a picture of the airborne prototype of ALISEO.

This Sagnac interferometer produces a fixed (stationary) pattern of interference fringes of equal thickness (Fizeau fringes). The Optical Path Difference (OPD) between the recombining beams linearly changes with the angle (slope) of the entering ray onto the instrument optical axis.

Due to the absence of entrance slit the device acquires the image of the target superimposed to a fixed pattern of interference fringes.

The prototype flew on July 29, 2008 during a test campaign over the Tuscan countryside close to Borgo San Lorenzo (Florence, Italy). The flight was performed by a Groppo Folder, an ultra-light airplane shown in fig. 4.

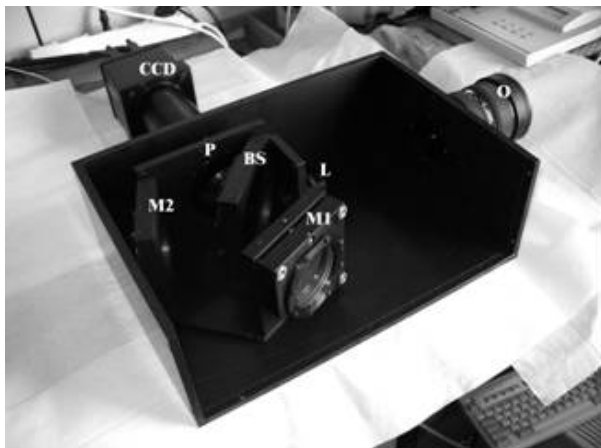


Fig. 3. Picture of the inner part of the imaging interferometer developed at our Institute



Fig. 4: Groppo Folder airplane

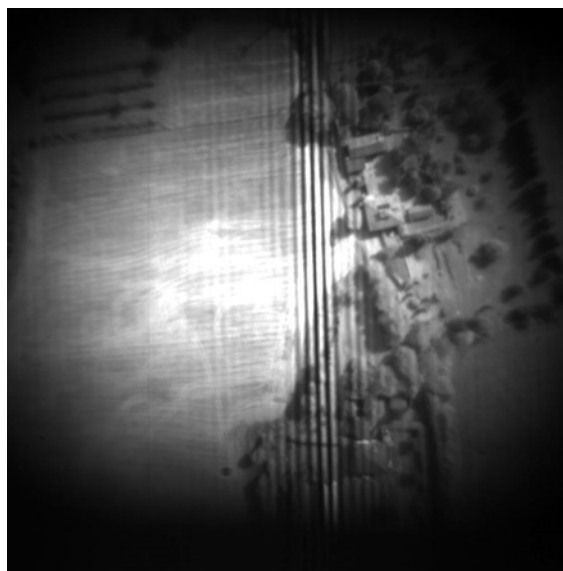
Fig. 5 displays two frames extracted from an acquisition performed the test campaign. The image sequence was acquired flying at an altitude of 500m.

Due to the low coherence of solar radiation, the fringes visibility (and their number) is limited to a small central region of the collected image. The dark central fringe corresponds to the null optical path difference between the two interfering rays.

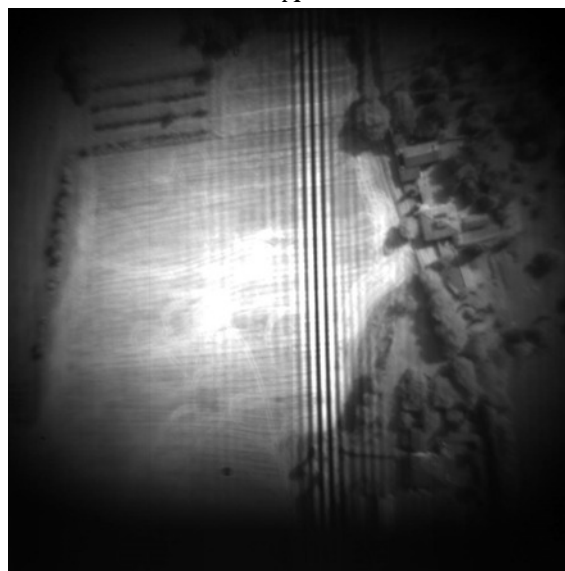
Fig.5a and 5b show the relative sensor-object motion along a 0.5sec time interval.

During a complete acquisition, each target's location crosses the entire interference pattern, hence the corresponding pixel is observed under different phase delays when the scene is framed repeatedly in time [6], [7]. The collected image sequence forms a 3-dim array of data (image stack). This data-cube is first processed in order to extract the complete interferogram of every target's point, and then it is cosine inverse transformed to yield a hyperspectral data-cube. Stack geometry is related to important characteristics of sensor and acquired data. As an instance, image sequence and target-sensor relative velocity govern the actual optical path difference

between consecutive sample of a retrieved interferogram.



A



B

Fig. 5: Two frames extracted from an airborne acquisition over countryside around Borgo San Lorenzo (Firenze).

2.1 Interferogram dispersion

The raw interferogram of the energy coming from a pixel of the observed scene is pre-filtered due to the finite pixel dimension p , and uniformly sampled in a region limited by the detector size D . The measured interferogram $\overline{i(x)}$ may be expressed as:

$$\overline{i(x)} \approx \left[i(OPD(x)) * \text{rect}\left(\frac{x}{p}\right) \right] \text{comb}\left(\frac{x}{p}\right) \text{rect}\left(\frac{x}{D}\right) \quad (1)$$

x being the pixel position. It can be easily shown that the relationship between OPD and the entering ray direction ϑ is linear, as long as the device FOV is not superior to a few degrees:

$$OPD(\vartheta) = \frac{a}{f}(j - j_0)p = \frac{a}{f}x \quad (2)$$

a being the proportionality constant between OPD and ϑ , and f the focal plane distance. The constant a is related to the maximum digitised optical path difference OPD_{\max} and to the maximum angle ϑ_{\max} .

The raw interferogram is constituted by points $(x, DN(x))$, which indicate the pixel position on the detector and the corresponding electronic signal expressed in digital number. According to Shannon's theorem the interferogram sampling frequency k_s should be greater than the full bandwidth k_{\max} of the concerned signal:

$$k_s = \frac{1}{2 \delta OPD} \geq k_{\max} \quad (3)$$

In view of Eq.3 the minimum wavelength λ_{\min} we can reconstruct avoiding signal aliasing is $\lambda_{\min} = 2\delta OPD$, δOPD being the optical path difference subtended by two adjacent pixels. Otherwise speaking, the greatest wavenumber (i.e. the shortest wavelength) one can observe without aliasing is that wavelength for which not less than two detector elements cover one fringe cycle. All wavelengths longer than this limit will have their fringe cycles sampled by more than two detector elements.

2.2 Spectrum recovery

As known the spectrum of any pixels have to be reconstructed by means of an inverse cosine transform; i.e. the real part of the inverse Fourier transform. A possible critical point for performing this transformation is constituted by a not perfect knowledge of the factor $\gamma = \frac{a}{f}$, which is essential for

computing the OPD corresponding to a generic position x . As long as some error affects the knowledge of the factor γ the calculated inverse transform will lack of accuracy, possibly originating a wrong estimate of the pixel spectrum. A preliminary issue is allowing some theoretical modelling that can account for this type of uncertainty. Let us suppose that the value $\tilde{\gamma}$ available for the factor γ be erroneous, then the retrieved spectrum $\tilde{I}(k)$ differs

from the true one $I(k)$ as stated by the following equations:

$$\tilde{I}(k) = \text{Re} \left\{ \int_{\Re} i_{id}(x) e^{2\pi j k \tilde{\gamma} x} dx \right\} \quad (4)$$

$$\tilde{I}(k) = \text{Re} \left\{ \int_{\Re} i_{id}(x) e^{2\pi j \tilde{k} \gamma x} dx \right\} \quad (5)$$

\tilde{k} being:

$$\tilde{k} = k \frac{\tilde{\gamma}}{\gamma} \Rightarrow \tilde{\lambda} = \lambda \frac{\gamma}{\tilde{\gamma}} \quad (6)$$

It can be easily shown that the :

$$\tilde{I}(k) = I(\tilde{k}) \quad (7)$$

Therefore, an error in the interferogram dispersion gives rise to a corresponding wavelength scale error in the spectrum domain. Let us note that the difference $I(k) - I(\tilde{k})$ may become large around narrow absorption lines due to the atmosphere or the observed target. A second trouble that can affect the inverse transform procedure is connected with the exact knowledge of the interferogram's centre. It is evident that an error affecting the central position of the interferogram produces a well-known cosine-like modulation of the inverse cosine transform.

Simulation of spectra retrieving is shown in Fig. 6. Estimated spectrum for a rect() source (500 nm until 800 nm) as observed with a 20 mm BK7 beam-splitter. A specific algorithm has been applied for compensating the spectral dispersion of the BK7 refraction index.

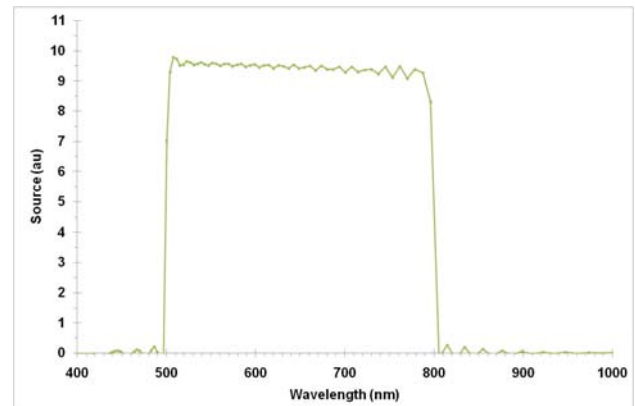


Fig. 6 Simulation of spectra retrieving

3. EXPERIMENTAL ACTIVITY

3.1 Calibration procedure

Preliminary measurements have been carried out in order to calibrate the interferometer response. Two dyed He-Ne lasers ($\lambda^{red} = 632.8nm$ and $\lambda^{green} = 543.2nm$) have been employed for illuminating a double planar diffuser in order to obtain a homogeneous and isotropic radiation distribution inside the instrument FOV. Fig. 7 shows a single image-frame obtained with the green laser source. The high number of these interference fringes is related to the high intrinsic coherence-degree of the employed radiation source.

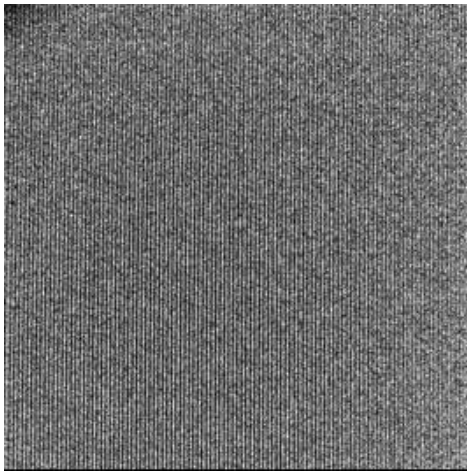


Fig. 7: Raw image (grey scale) obtained illuminating a double planar diffuser with a green He-Ne laser. The image is filled with a pattern of across-track interference fringes of equal thickness

The pre-processed interferogram should have a null-mean, starting and ending tails approaching to zero, and any optical artefact removed. In order to achieve these characteristics, we have elaborated a general scheme which is based on the following main steps [8], [9]:

- dark signal subtraction to account bias and noise in the detector electronic stage;
- instrument spatial response compensation to remove saturated pixels, hot and cold pixels, and fixed-pattern noise;
- geometrical and radiometric distortion correction to remove effects of vignetting and spatial shift of the fringes;
- DC-offset subtraction;
- apodization to avoid "Gibbs effect" (ringing phenomenon);

- cosine inverse transform to retrieve the un-calibrated at-sensor radiance spectrum;

The spectral dispersion of optical path differences, which is due to the dispersion law of the refractive index of the beam splitter makes the calibration of the OPD axis really a complex task. When a broad spectral range is exploited, the OPD values may significantly depend upon the spectrum of the observed target. Thus the inversion model of the interferogram as well as the spectral calibration of the sensor might be difficult and their interpretation ambiguous.

The uncalibrated radiance, retrieved applying gaussian apodization are plotted versus wavelengths in Fig. 8. Due to the circumstance that the employed spectral source may be approximated to an impulse-like radiation source, this measurement is also a good test to estimate the instrument spectral resolution: roughly 23 nm at 632 nm. Let us note that the spectral resolution has been lowered due to apodization. and OPD spectral dispersion.

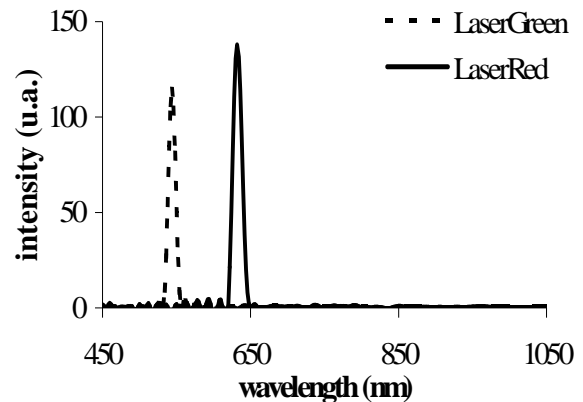


Fig. 8. Uncalibrated spectra of at-sensor radiance retrieved by cosine transforming the interferograms plotted in Fig. 4.

3.2 SNR estimates

We have executed 40 measurements employing a 600W halogen lamp, each measurement being constituted by 30 frames. The mean and the standard deviation have been computed for each pixel-sample, hence obtaining a set of 1024 mean and standard deviation values interferograms. The SNR and the noise amplitude have been so estimated, and their plots are shown in Fig. 9.

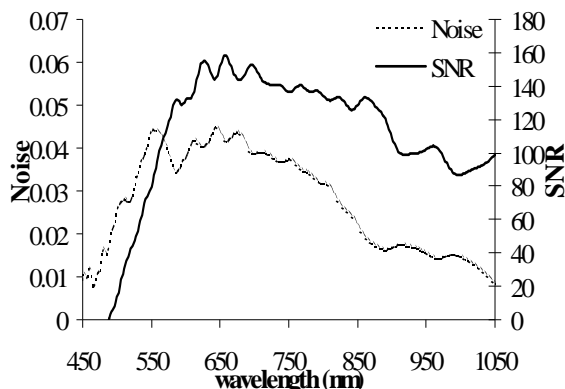


Fig. 9: Plot of SNR and noise amplitude (standard deviation) as computed from 40 interferograms collected observing the same radiation source.

2.3 Reflectance spectra reconstruction

Standard reflectance tiles together with diffusers doped with Holmium and Rare Earths have been used to check the reflectance spectra retrieved from ALISEO interferograms. For each tile a complete interferogram has been reconstructed, then the at-sensor radiance have been computed. Reflectance spectra are calculated taking as reference the radiance spectrum extracted from a Spectralon tile. Results of these measurements are plotted in Fig. 10.

Retrieved reflectance spectra have been used to verify the wavelength calibration of the instrument. The obtained results are in fair agreement with reference data. We suppose that partial departure of retrieved spectra from references is caused by the still insufficient compensation of the spectral dispersion of OPD.

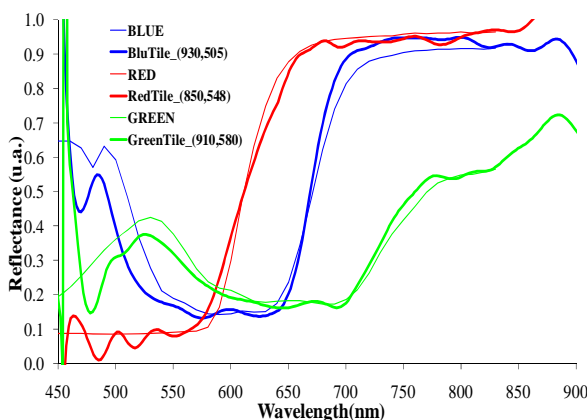


Fig. 10. Standard tiles reflectance spectra: Reconstructed spectra from measured interferograms are shown with a bold line. Labsphere reflectance spectra are plotted with a thin line.

5. CONCLUSIONS

In this paper an imaging interferometer prototype of the ALISEO sensor has been presented. The optical layout and the configuration of the instrument have been analysed, and the main differences with existing interferometers have been assessed. A procedure to retrieve the at-sensor radiance has been presented and discussed. Experimental investigation carried out at our Institute allowed us to measure the interferometer spectral resolution and the range of wavelengths that can be reconstructed. Future activities will be devoted to the implementation of a procedure for performing atmospheric corrections of the acquired images on board of an aircraft.

6. REFERENCES

1. Harnisch W. B., E. Hartman, W. Holota, M. Melf, W. Posselt, M. Rost, M. Steiner, H. O. Tittel, W. Weihs, 2002. Compact Fourier Transform Imaging Spectrometer, ESA-CN 14540/00/NL/WK, Proposal No. A.1999-0366-0-1, 1.2.2000 – 31.3.2002.
2. Jacquinot P., The luminosity of spectrometers with Prisms, Grating, or Fabry-Perot Etalons, *J. Opt. Soc. Am.*, 44, pp. 761 – 765.
3. Griffiths P.R., H. J. Sloane, and R. W. Hannah, Interferometers vs Monochromators: separating the optical and digital advantages, *Applied Spectroscopy*, 31, pp. 485 – 495, 1977.
4. Persky, M. J., A review of spaceborne infrared Fourier transform spectrometers for remote sensing, *Review of Scientific Instruments*, 66, pp. 4763 – 4797, 1995.
5. Sellar, R. G. and G. D. Boreman, Limiting aspect ratio of Sagnac inteferometers, *Optical Engineering*, 42, pp.3320 – 3325, 2003.
6. Barducci A., P. Marconi, I. Pippi, M. Poggesi, Simulation of the Performance of a Stationary Imaging Interferometer for High Resolution Monitoring of the Earth, In *Sensors, Systems, and Next-Generation Satellites VII, Proc. SPIE 4540*, pp. 112 – 121, 2001.
7. Barducci A., F. Casini, F. Castagnoli, P. Marconi, M. Morandi, I. Pippi, Performance assessment of a Stationary Interferometer for High-Resolution Remote Sensing, in *Algorithms and Technologies for Multispectral, Hyperspectral, and*

Ultraspectral Imagery VIII, Proc. SPIE 4725, pp. 547 – 555, 2002.

8. Barducci A., I. Pippi, Analysis and rejection of systematic disturbances in hyperspectral remotely sensed images of the Earth, *Applied Optics*, 40, pp. 1464 – 1477, 2001.

9. Barducci A., F. Castagnoli, P. Marcoianni, I.Pippi, The ALISEO instrument: further improvements of calibration methods and assessment of interferometer response, In *"Sensors, Systems, and Next-Generation Satellites XI"*, *SPIE 5978*, pp. 1K – 1-10, 2005.